Atmospheric effects and spurious signals in GPS analyses

P. Tregoning[1] and C. Watson[2]

[1] Improvements in the analyses of Global Positioning System (GPS) observations yield resolvable millimeter to submillimeter differences in coordinate estimates, thus providing sufficient resolution to distinguish subtle differences in analysis methodologies. Here we investigate the effects on site coordinates of using different approaches to modeling atmospheric loading deformation (ATML) and handling of tropospheric delays. The rigorous approach of using the time-varying Vienna Mapping Function 1 yields solutions with lower noise at a range of frequencies compared with solutions generated using empirical mapping functions. This is particularly evident when ATML is accounted for. Some improvement also arises from using improved a priori zenith hydrostatic delays (ZHD), with the combined effect being site-specific. Importantly, inadequacies in both mapping functions and a priori ZHDs not only introduce time-correlated noise but significant periodic terms at solar annual and semiannual periods. We find no significant difference between solutions where nontidal ATML is applied at the observation level rather than as a daily averaged value, but failing to model diurnal and semidiurnal tidal ATML at the observation level can introduce anomalous propagated signals with periods that closely match the GPS draconitic annual ($\sim$351.4 days) and semiannual period ($\sim$175.7 days). Exacerbated by not fixing ambiguities, these signals are evident in both stacked and single-site power spectra, with each tide contributing roughly equally to the dominant semiannual peak. The amplitude of the propagated signal reaches a maximum of 0.8 mm with a clear latitudinal dependence that is not correlated directly with locations of maximum tidal amplitude.

1. Introduction

[2] For over a decade the Global Positioning System (GPS) has been used to study geophysical phenomena manifesting as temporal changes of the Earth's crust and its atmosphere and oceans. The first most significant results related to plate tectonic motion, notably continental drift [e.g., *Feigl et al.*, 1993] and earthquake deformation [e.g., *Bock et al.*, 1993]. Better analysis techniques have led to improved accuracy which now permits GPS to be used to study, for example glacial isostatic adjustment [e.g., *Milne et al.*, 2001; *Sella et al.*, 2007], tide gauge stability [e.g., *Snay et al.*, 2007; *Wöppelmann et al.*, 2007], elastic deformation caused by atmospheric loading [e.g., *Tregoning and van Dam*, 2005a] and atmospheric remote sensing [e.g., *Bevis et al.*, 1992].

[3] Variations in the Earth's atmosphere introduce time-dependant changes to GPS antenna locations caused by mass loading [e.g., *van Dam et al.*, 1994]. In addition, variation in the water content of the atmosphere delays the incoming GPS observations as they propagate through the troposphere [e.g., *Bevis et al.*, 1992]. Recent improvements in GPS analyses have been achieved through improved modeling of atmospheric loading, the use of more sophisticated mathematical functions to relate the tropospheric delays in the zenith direction to the delay at any elevation angle and also through improved a priori values for zenith hydrostatic delays [e.g., *Boehm et al.*, 2006a]. Some of these analysis enhancements can be achieved through the use of simple, empirical formulae while others require more complicated procedures of utilizing and interpolating external data sources. It is thought that the added complexity of some of the new models, specifically those related to those handling atmospheric delays, is responsible for their slow uptake by the international community [*Steigenberger et al.*, 2009].

[4] The Vienna Mapping Function 1 (VMF1) [*Boehm and Schuh*, 2004; *Boehm et al.*, 2006a] utilizes time-dependent, spatially varying values for coefficients in the continued fraction form [*Herring*, 1992], where the coefficients are derived from ray tracing through pressure levels of the European Center for Medium-Range Weather Forecasts (ECMWF) operational analysis data. The global mapping function (GMF) is an empirical representation of the VMF1 that is readily implemented in existing software and that captures the first-order variations of the VMF1

---

[1]Research School of Earth Sciences, Australian National University, Canberra, ACT, Australia.
[2]Surveying and Spatial Science Group, School of Geography and Environmental Studies, University of Tasmania, Hobart, Tasmania, Australia.
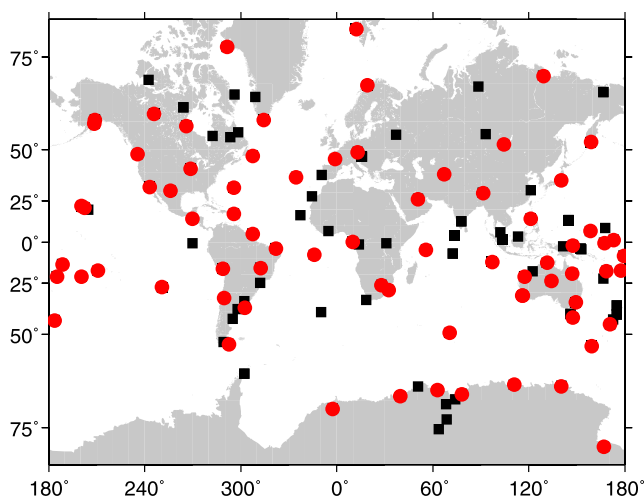
Figure 1. Locations of GPS sites included in the analysis (black squares). The 73 sites used in the in the noise analysis are shown as red circles.

[*Boehm et al.*, 2006b]. These two mapping functions are arguably the most accurate available at the present time. A question to address is whether there is merit in utilizing the more complicated models or whether the empirical approximations suffice.

[5] Of relevance to this issue is the fact that errors in the modeling of the tropospheric delay can be negatively correlated with atmospheric loading deformation (ATML) [e.g., *Tregoning and Herring*, 2006]. Studies of mapping functions and zenith hydrostatic delay (ZHD) interactions by *Kouba* [2008] and *Steigenberger et al.* [2009] did not apply ATML at the observation level. As stated by *Kouba* [2008] and *Steigenberger et al.* [2009], the uncertainty introduced by not modeling the ATML at the observation level limits the value of their conclusions.

[6] We focus this analysis on the question of whether the use of empirical functions to represent the temporal variations of the mapping function coefficients and surface pressure (used to calculate the a priori ZHD) yields results on a global scale of comparable quality to using actual time-varying coefficients and ZHD derived directly from numerical weather models. To this end, we address the question of whether the VMF1 performs better than empirical mapping functions when all other analysis strategies are held constant, then assess separately the impact of different strategies for the a priori modeling of the ZHD using the VMF1 in all cases. To better understand the interaction between estimating tropospheric delays and ATML, we generate the above solutions using various strategies to account for ATML.

[7] We first review the different GPS modeling strategies with respect to mapping functions, the treatment of a priori ZHD and the modeling of ATML as utilized in this paper. We begin our analysis by revisiting approaches used to handle ATML within GPS analyses, comparing the application of filtered ATML applied at the observation level or as a daily averaged value, both with and without the inclusion of the tidal components of the deformation signal. We then assess the influence of different mapping function/ZHD combinations as well as with and without ATML applied. Our assessments of solution quality go beyond the

comparison of the RMS of each coordinate component time series: we consider the time correlated noise structure of both the raw time series and those produced by differencing time series generated using slightly different analysis strategies. Analysis of stacked power spectra and power law noise metrics has enabled us to describe and quantify subtle differences in GPS analysis strategies in terms of the reduction of white and coloured noise components as well as the magnitude of spurious propagated signals present in the time series.

2. GPS Modeling Strategies

[8] For the analysis presented in this paper, we have processed GPS observations from a globally distributed network of over 80 sites using a number of combinations and permutations of mapping functions, a priori ZHD modeling and application strategies dealing with ATML. Over 32,000 daily solutions of GPS data from 2000.0 to 2008.0 were generated. The GPS observations were analyzed using the GAMIT/GLOBK software [*Herring et al.*, 2008] as two, interwoven global sub networks of ~40 sites, each with at least five common sites between the two networks. Satellite state vectors, residual tropospheric delay estimates (every hour), atmospheric gradients (three N/S and three E/W per day) and Earth orientation parameters were estimated along with site coordinates. We used an elevation cutoff angle of 10° in all solutions and applied site-specific, elevation-dependent weighting of the observations based on an assessment of the postfit phase residuals. With one exception, we discuss in this paper only the ambiguity-fixed solutions, where generally ~90−95% of the phase ambiguities were resolved (post-2004 but 70−90% for the time period 2000−2004). For each solution, the loosely constrained daily subnetworks were combined in a second step where the terrestrial reference frame was defined by performing a six-parameter transformation of the coordinates of ~30 sites onto the ITRF2005 [*Altamimi et al.*, 2007]. The steps undertaken to realize the reference frame were identical for all solutions. The distribution of sites analyzed is shown in Figure 1.

[9] We restricted our detailed study of the noise characteristics and differences between solutions to only those sites with more than 3 years of data (not necessarily consecutive), with no known offsets caused by hardware changes, and with no known coseismic and/or postseismic deformation signals or identifiable effects of snow covering antennae. In some cases, only specific periods of data were used from sites affected by one or more of the effects previously mentioned (e.g., Cocos Islands is affected by the Sumatra-Andaman earthquakes in 2004/2005). In such cases, only data spans sufficiently long enough to meet our criteria were included.

[10] In this section, we describe the different analysis strategies adopted as summarized in Table 1. We subsequently use the solution numbers in Table 1 when discussing and interpreting differences between the various processing strategies.

2.1. Mapping Functions

[11] The retardation of the transmitted GPS signals through the troposphere is commonly divided into a hydro-

Table 1. Componentwise Global-Weighted Average Time Series Metrics

			White Noise Only Analysis						White and Power Law Noise Analysis								
Solution Strategies[a]			WN only			WN+Periodic			WN			PL Magnitude			Spectral Index		
No.	Tropo MF/ZHD	ATML Nontidal/Tidal	N	E	U	N	E	U	N	E	U	N	E	U	N	E	U
1	V/E	none/none	2.04	2.01	6.43	1.94	1.92	5.74	1.35	1.42	4.06	3.94	3.81	14.38	−0.79	−0.78	−0.82
2	G/G	none/none	2.03	1.99	6.29	1.92	1.91	5.61	1.34	1.40	4.06	3.96	3.76	13.23	−0.79	−0.78	−0.78
3	N/S	none/none	2.06	2.03	6.35	1.96	1.94	5.66	1.37	0.84	4.13	3.92	3.67	13.36	−0.78	−0.76	−0.78
4	V/E	nontidal/none	1.98	1.96	5.67	1.87	1.86	5.09	1.30	1.37	3.46	4.00	3.54	11.11	−0.90	−0.84	−0.78
5	V/E	partial/none[b]	1.98	1.95	5.67	1.88	1.86	5.10	1.28	1.38	3.45	4.05	3.56	11.24	−0.90	−0.84	−0.78
6	V/E	none/S1+S2	2.04	2.00	6.43	1.93	1.92	5.73	1.36	1.41	4.13	3.97	3.83	14.32	−0.80	−0.79	−0.82
7	V/E	daily avg/S1+S2	1.98	1.97	5.68	1.88	1.87	5.10	1.30	1.37	3.48	3.98	3.57	11.03	−0.84	−0.83	−0.77
8	G/G	daily avg/S1+S2	1.98	1.97	6.01	1.88	1.86	5.47	1.28	1.38	3.90	4.03	3.83	12.23	−0.85	−0.91	−0.76
9	V/E	nontidal/S1+S2	1.97	1.97	5.68	1.87	1.86	5.10	1.30	1.37	3.46	4.00	3.54	10.88	−0.91	−0.82	−0.78
10	V/G	nontidal/S1+S2	1.98	1.96	5.71	1.87	1.86	5.13	1.30	1.37	3.55	4.01	3.55	11.60	−0.85	−0.84	−0.76
11	V/S	nontidal/S1+S2	1.98	1.97	5.71	1.87	1.86	5.13	1.29	1.38	3.53	4.01	3.55	10.65	−0.85	−0.83	−0.71
12	G/E	nontidal/S1+S2	1.98	1.96	5.93	1.87	1.86	5.39	1.31	1.37	3.91	3.99	3.56	11.41	−0.88	−0.83	−0.73
13	G/G	nontidal/S1+S2	1.98	1.96	6.02	1.88	1.86	5.48	1.28	1.36	3.89	4.01	3.53	12.27	−0.85	−0.82	−0.76
14	G/S	nontidal/S1+S2	1.99	1.97	6.02	1.88	1.86	5.49	1.30	1.36	3.93	4.01	3.58	12.21	−0.84	−0.83	−0.75
15	N/E	nontidal/S1+S2	1.99	1.98	5.94	1.89	1.88	5.39	1.32	1.38	3.87	4.01	3.57	11.33	−0.84	−0.82	−0.72
16	N/S	nontidal/S1+S2	2.00	1.99	5.98	1.89	1.89	5.46	1.33	1.40	3.88	4.05	3.64	12.13	−0.89	−0.83	−0.76

[a]For ease of interpretation, the solutions are coded by solution number, mapping function/ZHD, long-period ATML/tidal ATML. The mapping function (MF) is abbreviated to V:VMF1, G:GMF and N:NMF. The choice of ZHD is abbreviated to E:ECMWF, G:GPT and S:STP. The treatment of nontidal ATML and tidal ATML is indicated.

[b]The tides are partially represented in the 6-hourly values rather than being modeled with a periodic function.

static and a wet component, as described in detail by for example [*Herring*, 1992; *Bevis et al.*, 1992]. The corrections to a priori total tropospheric delays are made in GPS software using the partial derivative that relates the wet delay to the observed phase. Therefore, any errors that exist in the a priori zenith hydrostatic delay are corrected using the wrong partial derivative [e.g., *Tregoning and Herring*, 2006; *Kouba*, 2008; *Steigenberger et al.*, 2009].

[12] The New Mapping Function (NMF) [*Niell*, 1996] was one of the first time-varying mapping functions and was regarded as the most accurate mapping function available. The development of the VMF1 [*Boehm et al.*, 2006a] involved deriving time-varying coefficients of the mapping functions (with separate coefficients for the hydrostatic and wet functions) from the ECMWF global weather model. The GMF [*Boehm et al.*, 2006b] is an empirical expression of the VMF1, designed to be more easily implemented into existing software packages. We generated our solutions using each of the NMF, GMF and VMF1 (see Table 1).

2.2. A Priori Hydrostatic Delay Modeling

[13] The zenith hydrostatic delay (ZHD) can be modeled if a priori knowledge of the surface atmospheric pressure is known. The important element is the a priori surface atmospheric pressure that is used in the equation of *Saastamoinen* [1972] to model the a priori zenith hydrostatic delay. The mathematical formulae have been described extensively elsewhere [*Saastamoinen*, 1972] and will not be repeated here. As discussed in this section, the different methods of modeling surface pressure categorize the possible ZHD strategies adopted in any GPS analysis.

2.2.1. Standard Sea Level Pressure

[14] Many analysts have used a simple model of a constant, "standard" sea level temperature and pressure of 20°C and 1013.25 hPa, then adjusted the pressure value to account for the height of the GPS site above sea level [e.g., *Dach et al.*, 2007; *Zhang et al.*, 1997; *Dong et al.*, 2002; *Williams et al.*, 2004]. While acknowledging that this approach is now obsolete, we include the approach (abbre-

viated as STP) to demonstrate how the use of the more recent use of time varying a priori pressure values and ECMWF-derived ZHD has affected the resulting solutions.

2.2.2. Global Pressure and Temperature Model

[15] *Boehm et al.* [2007] developed the Global Pressure and Temperature (GPT) model, a degree 9 spherical harmonic representation of global atmospheric surface pressure that varies temporally as well as spatially. *Tregoning and Herring* [2006] showed that the use of the GPT over STP changed the station height estimates by up to 10 mm, especially in Antarctica. The GPT is an empirical formula that is readily implemented without any need for actual observation-based input files.

2.2.3. ECMWF-Derived Values

[16] At the same time as estimating coefficients for the VMF1, *Boehm et al.* [2006a] generate values for the ZHD from the pressure fields of the ECMWF. This provides another alternate means of deriving a priori ZHD values and has been used in the analysis of GPS data [*Wöppelmann et al.*, 2007; *Kouba*, 2008; *Tregoning et al.*, 2009]. Implementation of ECMWF-derived a priori hydrostatic values requires the use of input files of time-varying ZHD (available from http://www.hg.tuwien.ac.at/~ecmwf1) on global grids, along with the orthometric height to which the grid points refer. We first adjust the ZHD values at the four nearest grid nodes to the height of the GPS station (using the expressions of *Saastamoinen* [1972] to relate changes in ZHD to changes in height), then bilinearly interpolate the four values to derive the ZHD value at the site. We abbreviate this strategy for ZHD as ECMWF throughout this paper.

2.3. Atmospheric Loading

[17] That variations in atmospheric pressure cause elastic deformation of the surface of the Earth has been understood for over a century [*Darwin*, 1882]. Early space-geodetic studies were made using the very long baseline interferometry (VLBI) technique [*van Dam and Herring*, 1994] and more recently both horizontal and vertical deformation have
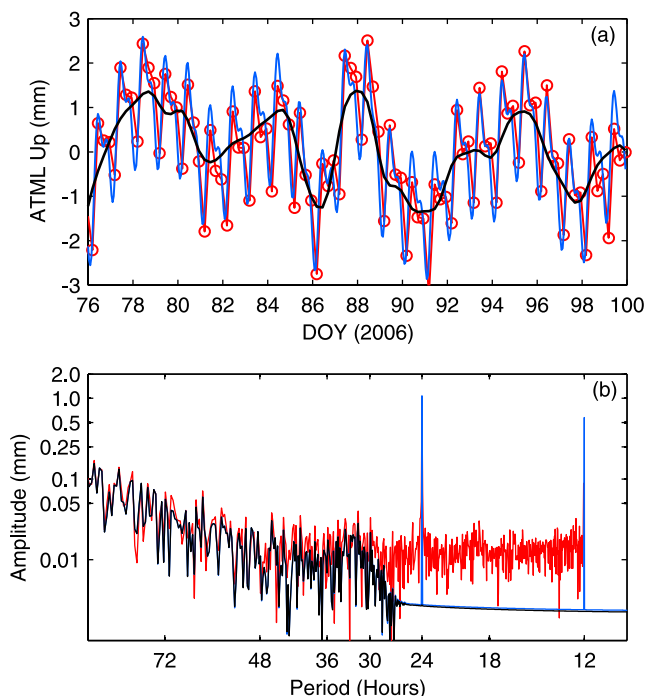
Figure 2. (a) Example time series of atmospheric loading deformation in the up component at Bahrain for the partial model used by *Tregoning and van Dam* [2005a] (red), our nontidal model (black) and our nontidal plus S1+S2 model (blue). (b) Power spectra of partial (red), nontidal (black) and nontidal plus S1+S2 (blue).

been detected using VLBI with corrections now applied at the observation level [*Petrov and Boy*, 2004]. *Tregoning and van Dam* [2005a] applied corrections at the observation level in GPS analyses and showed some improvement in the repeatability of height estimates with this approach when compared to simply applying a daily average correction after the station coordinates had been estimated. They also showed that applying diurnal and semidiurnal atmospheric loading worsened the solutions but suggested that this was due to the continued presence of residual or partial tidal loading in their so-called ''nontidal'' component. Other analysts have applied ATML at the observation level using the GAMIT software [e.g., *Wöppelmann et al.*, 2007; *Watson et al.*, 2006] but, to our knowledge, no studies using other GPS software packages have yet applied ATML at the observation level.

[18] The process of convolving surface atmospheric pressure variations with Green's functions to generate estimates of horizontal and vertical deformations has been described extensively elsewhere [e.g., *Farrell*, 1972; *Petrov and Boy*, 2004] and will not be repeated here. The surface pressure values used in the convolutions are generally sourced from either ECMWF [e.g., *Boehm et al.*, 2006a] or National Centers for Environment Prediction (NCEP) reanalysis products [e.g., *Petrov and Boy*, 2004; *Tregoning and van Dam*, 2005a]. These fields are provided every 6 h, the Nyquist frequency for the semidiurnal atmospheric tide, and still contain power at the tidal frequencies. In this section, we describe the different strategies used to handle both the

nontidal and tidal components of ATML in our GPS analyses.

2.3.1. Nontidal ATML

[19] *Petrov and Boy* [2004] attempted to remove the tidal power from the 6-hourly atmospheric pressure values by estimating sinusoidal parameters at each grid node before convolving surface pressure into elastic deformation, while *Tregoning and van Dam* [2005a] simply convolved the NCEP pressure values, including some components of the tidal pressure. In both cases, energy at tidal frequencies remained in the nontidal ATML deformation (Figure 2, see also Figures 1 and 2 of *Petrov and Boy* [2004] and Figure 2 of *Tregoning and van Dam* [2005a]). Given the under sampling and often erroneous representation of the atmospheric tides in 6-hourly reanalysis products [e.g., *Ponte and Ray*, 2002], we chose to filter the convolved deformation estimates of *Tregoning and van Dam* [2005a] using a low-pass Butterworth filter of order 20 to remove the tidal energy from the deformation computations. This filtering process has a frequency cutoff of just below 1 cycle per day, thus in Figure 2 we see only the low-frequency variations in the filtered ATML time series with virtually no energy remaining in the diurnal and semidiurnal tidal band. We define this filtered ATML as nontidal in this paper. We apply the nontidal ATML at the observation level in our GPS analyses, linearly interpolating between the 6-hourly nontidal deformation estimates.

2.3.2. Daily Averaged Nontidal ATML

[20] An alternate approach to applying ATML at the observation level is to apply a daily averaged value of nontidal ATML to the estimated coordinates of each site after the reduction of the raw GPS observations. We also adopted this strategy for comparison purposes in our analyses (solution 7 in Table 1, abbreviated as ''daily avg''). This was implemented by applying the daily averaged nontidal ATML values to the site coordinates in the centre of mass (CM) frame prior to defining the terrestrial reference frame. It is important that the daily averaged ATML be applied prior to the definition of the reference frame, otherwise, the unmodeled ATML could corrupt the transformation process since the estimates of the site coordinates still contain the loading deformation signal. In particular, estimating a scale factor in the transformation process in the presence of unmodeled ATML leads to erroneous coordinate estimates [*Tregoning and van Dam*, 2005b].

2.3.3. Tidal ATML

[21] To account for the tidal component of ATML, we modeled the elastic deformation associated with the solar diurnal (S1) and semidiurnal (S2) atmospheric tides using the annual mean model of *Ponte and Ray* [2002]. This follows the procedures of, for example *Petrov and Boy* [2004] and *Tregoning and van Dam* [2005a]. We did not invoke an inverted barometer assumption; rather, the oceans are considered not to respond at subdaily timescales to the tidal variations in atmospheric pressure. The tidal ATML, abbreviated in our analyses as ''S1+S2'' is applied at the observation level by bilinearly interpolating a global grid of model coefficients to the site location and then computing the combined tide at the time of each observation. The amplitudes of the S1 and S2 tidal deformations in the vertical component reach ∼1 mm at equatorial sites, reducing to negligible deformation at the poles.

2.3.4. Partial Tidal ATML

[22] The residual "partial" component of atmospheric tidal deformation is clearly apparent in the example time series of ATML at Bahrain shown in Figure 2a, where the diurnal and semidiurnal periodic variations are visible, superimposed over longer wavelength synoptic pressure variations. This is the so-called nontidal ATML model applied by *Tregoning and van Dam* [2005a] which we call in this paper "partial ATML" since it clearly contains some of the deformation signal at tidal frequencies. The corresponding power spectrum in the ATML time series at Bahrain is shown in Figure 2b.

[23] The deformation calculated from the addition of nontidal plus S1+S2 deformation (Figure 2b) does not pass through all the 6-hourly points of the partial ATML time series. This is due in part to the data assimilation process used in the generation of 6-hourly NCEP pressure fields which is known to bias the tidal components of atmospheric pressure [*Ponte and Ray*, 2002]. In addition, the tidal model applied in our analysis is that derived from ECMWF reanalysis products [*Ponte and Ray*, 2002] rather than the NCEP data which might induce a small difference in deformation estimates.

3. Assessing the Quality of Solutions

[24] The approach that the "best" model is the one that produces the smallest RMS has been used to assess the effectiveness of applying atmospheric loading [e.g., *van Dam and Herring*, 1994; *Petrov and Boy*, 2004; *Tregoning and van Dam*, 2005a]. The general metric used by each of these studies has been that a model and/or analysis approach is superior if the RMS about a linear regression or mean is smaller than that which results from some other approach. However, this assumes that there are no other nonlinear signals remaining in the coordinate time series. If it were the case that some other geophysical signals were present, then the most accurate atmospheric model(s) would be the one(s) that left the clearest definition of the remaining geophysical signal, rather than just the one(s) that produced the smallest RMS around a linear fit. In particular, if two effects are interfering destructively, then applying a model of only one of the effects will make the solutions appear worse, even though the model applied might well be perfect. How then should one assess which mapping function is more accurate, or how best to apply ATML?

[25] Recently, attention has focused on characterizing the time correlated noise structure evident within GPS time series. Earlier studies by *Zhang et al.* [1997] and *Mao et al.* [1999] highlighted that a complete treatment of the time-correlated noise characteristics is required in order to generate meaningful and realistic estimates of parameter uncertainties. *Williams et al.* [2004] made substantial progress providing a global analysis of white noise and power law noise components present in GPS time series.

[26] In this paper, we use the CATS software [*Williams*, 2008] to undertake a range of analyses on both the time series of individual solutions (Table 1) and differenced series generated by differencing common epochs from two solutions of interest. All coordinate components were processed using a white noise only model, a white noise model plus the addition of solving for annual (365.25 days) and semiannual (365.25/2 days) periodic terms, and a complete white noise plus power law noise model (including the annual and semiannual terms). Each analysis solves for the time series offset and trend, in addition to periodic signal components (when included) and, importantly, noise magnitudes, uncertainties and spectral indices (in the case of the power law analysis).

[27] We summarize these time series metrics by computing the weighted means across the global network, effectively defining a solution/componentwise statistical data set suitable for comparing different analysis strategies (Table 1). We propose that an optimal solution will be one that enables the most precise determination of time series parameters of geophysical interest, namely site offset, velocity and coefficients of periodic site displacement. Ideally, the noise structure of such a solution will contain solely white noise, yet in practice will include a coloured noise component of the smallest possible magnitude. The solution will also be ideally free of spurious signals at periods of geophysical interest. Put simply, we seek the solution that will generate the most accurate estimates of remaining geophysical signals.

[28] To assist in the comparison of analysis strategies, we supplement the time series metrics with globally stacked power spectra computed for each coordinate component using the Lomb-Scargle periodogram [*Scargle*, 1982], as implemented according to *Press et al.* [1992] with an oversampling factor of 4. Prior to stacking, the power spectra for each time series are normalized by variances of 14 mm^2, 25 mm^2 and 47 mm^2 for the north, east and up components, respectively, in order to aid the direct comparison between solutions. These variances represent the global average variances for each coordinate component from the VMF1/ECMWF nontidal plus S1+S2 solution. The stacked power spectra were also computed for a range of differenced time series to aid in the identification of common mode noise structures between solution types, that is, changes in noise structure caused by analysis strategy choices.

[29] Throughout the rest of the paper we review time series metrics summarized in Table 1, referring simultaneously to stacked power spectra of individual and differenced time series in order to characterize and contrast the properties of various solutions. Importantly, we augment these results with estimates of the amplitudes of introduced periodic signals which are generated when using different combinations of mapping function, a priori ZHD and tidal ATML.

4. Results

4.1. Atmospheric Loading

[30] In this section we address the issues of whether nontidal ATML should be applied at the observation level or whether applying a posteriori a daily averaged correction is sufficiently accurate. We also investigate the effects of different strategies for handling the tidal ATML deformation. We calculate and interpret differences between solutions where the mapping function and a priori ZHD modeling (plus all other analysis strategies) are kept the same. That is, only the treatment of the ATML is varied. We compare time series metrics (Table 1) before assessing in
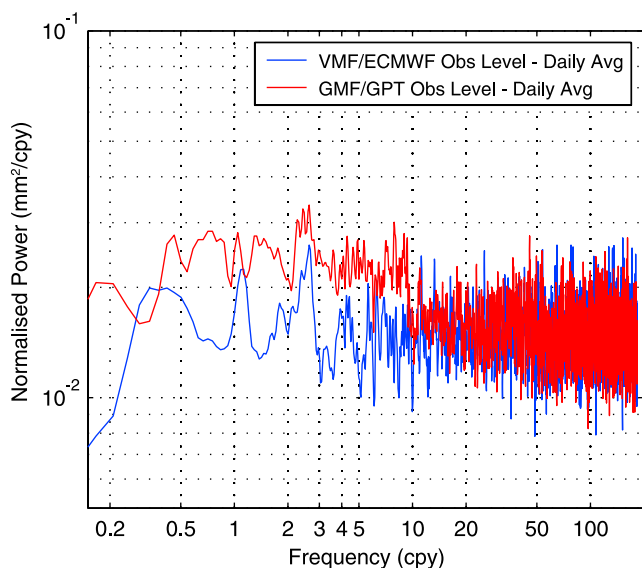
Figure 3. Stacked spectra showing the differences in the up component between applying nontidal ATML at the observation level or as a daily averaged value. Red line shows VMF1/ECMWF (solution 9 minus solution 7) and the blue line shows GMF/GPT (solution 13 minus solution 8).

greater detail the application of ATML at the observation level versus daily averaged, and subsequently investigating the influence of tidal ATML.

4.1.1. Time Series Metrics

[31] As expected, the solution-averaged white noise estimates are highest when no ATML is modeled (solutions 1, 2, 3 and 6). This confirms previous results and simply demonstrates that GPS coordinate estimates are sensitive to the elastic deformation of the Earth caused by temporal changes in atmospheric pressure. Given the seasonal timescales associated with pressure variations, it is also an expected result that the white noise only magnitudes are reduced when estimating annual and semiannual periodic terms. This improvement is seen across all components, with the largest improvement, as expected, in the vertical component with a white noise magnitude reduction from 6.43 to 5.74 mm (~2.9 mm in quadrature).

[32] Spectral indices for solution 1 indicate all components are marginally "whiter" in comparison to flicker noise (having a spectral index of −1), with the up component marginally whiter than north and east. We note that just applying the tidal components (solution 6) (i.e., not applying the nontidal ATML), worsens the solution across all components with respect to power law magnitude, and likewise for north and up with respect to white noise magnitude. This is addressed in greater detail in section 4.1.3.

[33] When applying the nontidal component of ATML (using either the partial, nontidal or daily averaged application), we observe the expected reduction in white and power law noise magnitudes. The ratio of noise magnitude between north and east to up is now comparable between white and power law magnitudes. Curiously, the modeling of the nontidal component of ATML (using the different strategies in solutions 4, 5, 7 and 9) marginally increases the spectral index, particularly for north and east, moving the

noise structure very close to flicker noise. This may be indicative of the application of ATML shifting the frequency at which coloured noise dominates the time series. The differences between solutions 4, 5, 7 and 9 are however quite subtle. Assuming that the best solution is that with the smallest power law magnitude, solution 9 (nontidal plus S1+S2) appears superior. We investigate these solutions in further detail throughout sections 4.1.2 and 4.1.3.

4.1.2. Daily Average or Observation Level ATML

[34] Should nontidal ATML be applied at the observation level or as a daily averaged value? The latter is potentially more attractive, as existing solutions can simply be corrected for loading effects without requiring any reprocessing of raw data, but does simplicity come at a cost of accuracy? To address this, we study coordinate differences of solutions with the same mapping function, a priori ZHD and tidal ATML applied at the observation level but where the nontidal ATML was applied either at the observation level or as an a posteriori correction in the CM frame prior to aligning the networks with the ITRF2005 terrestrial reference frame.

[35] It has been shown previously [e.g., *Tregoning and Herring*, 2006; *Steigenberger et al.*, 2009] that destructive interference can occur between errors in a priori ZHD and unmodeled ATML. This can result in a height error that is smaller than either of the two effects. If ATML is applied as a daily averaged correction once the observations have been reduced, then the full ZHD error will become visible in the solution. When ATML is applied at the observation level, the destructive interference is mitigated at the time of reducing the observations, and the resulting solutions will also contain the full effect of the a priori ZHD error. To test this, we computed coordinate differences from our solutions applying ATML either at the observation level or as a daily averaged value using the empirical approaches of GMF/GPT and also the more rigorous approaches of VMF1/ECMWF.

[36] In the VMF1/ECMWF case (solutions 7 and 9), there is negligible difference between the white noise only analyses. In the combined noise analysis, we again see negligible change to the white noise magnitudes, and marginal reductions in power law magnitudes for east and up for the solution with observation level application of ATML. The differences are small and statistically insignificant (the typical standard error about the weighted mean powerlaw magnitude in Table 1 is ~0.05, ~0.07 and ~0.15 for north, east and up, respectively).

[37] The stacked power spectrum of the VMF1/ECMWF solution differences (observation level minus daily average) shows very little difference between the two solutions, with the spectrum closely resembling white noise (Figure 3, up component only). There is slight evidence for increased power at ~1 and ~2.75 cpy, respectively, but these are not significant.

[38] When using the less accurate mapping function and ZHD of GMF/GPT the differences in white and power law noise are also small and insignificant. The power spectrum of the height differences between solutions with ATML applied at the observation level or as a daily averaged value (solutions 8 and 13) shows some structure at lower frequencies (Figure 3, blue curve); however, this equates to less than 0.1 mm in amplitude. Thus, we conclude that there is
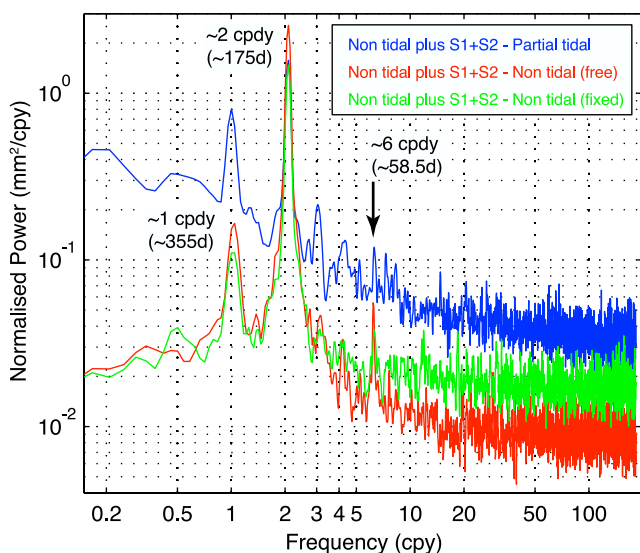
Figure 4. Stacked spectra showing the differences in the up component between approaches for accounting for tidal atmospheric loading deformation. Blue line shows nontidal plus S1+S2 (solution 9) minus partial (solution 5); Green line shows nontidal plus S1+S2 (solution 9) minus nontidal plus none (solution 4), and red line is same as for green but without fixing ambiguities in either solution.

no discernable difference in height estimates between applying ATML at the observation level or as a daily averaged value.

4.1.3. Tidal ATML

[39] In this section we address different ways of modeling the tidal components of ATML. In all cases we use the VMF1 mapping function and apriori ZHD derived from ECMWF and compute differences between solutions where the tidal ATML is either partially represented through the 6-hourly NCEP pressure values, not modeled at all or modeled by the periodic functions of *Ponte and Ray* [2002].

[40] From an assessment of the white noise only analysis, there is little to distinguish between our solutions that handle the tidal components of ATML differently (solutions 4, 5 and 9, Table 1). The power law metrics however show a considerable increase in power law magnitude for the partial solution across the north and up components, with a marginal reduction in east. As shown in Figure 2, the 6-hourly data spacing and undersampling of the S2 atmospheric tide can lead to a strange representation of the tidal components in the partial ATML time series. The stacked power spectrum in the up component of the difference between the nontidal plus S1+S2 and partial solutions (solution 9 minus 5, blue curve in Figure 4) shows a considerable time-correlated noise component. The driver for this change is purely the propagation of the non sinusoidal difference between the S1+S2 and partial tidal ATML, highlighting that a nonsinusoidal, subdaily periodic signal has the ability to propagate across a broad frequency band (<20 cpy), thereby increasing the power law noise component of a time series.

[41] Interestingly, the stacked spectra of the above differenced time series yield clear peaks at around (in decreasing magnitude) ~2 cpy, ~1 cpy and ~3 cpy with a trailing comb of harmonics that are barely distinguishable

from the noise floor. The dominant peaks present in the difference of solution 9 minus solution 5 are also evident, with improved frequency resolution, in the comparison of the difference between nontidal plus S1+S2 and nontidal only (solution 9 minus 4, green curve in Figure 4). The spectrum for this difference is much whiter with very little slope that would indicate the presence of time-correlated noise. This shows that failing to model tidal ATML with S1 and S2 sinusoidal signals will lead to the propagation of these signals to very specific low-frequency signals but without adding significant time-correlated noise.

[42] On closer inspection, the dominant peaks do not fall at harmonics of the solar year (365.25 days), but slightly less (~350–355 days). The dominant semiannual peak has a well defined period of ~175 days (compare 182.6 days for the solar semiannual period). Previous theoretical studies by *Penna and Stewart* [2003] and *Stewart et al.* [2005] predicted the propagation of a mismodeled S2 signal to a period of 182.63 days. Using real data but within a precise-point-positioning analysis environment, *Penna et al.* [2007] found that an introduced error in S2 propagated to an average period of ~176 days (from a total of eight sites included in their analysis). They explained the difference from solar semiannual period on the "perfect" orbital repeat time adopted in the *Stewart et al.* [2005] predictions.

[43] We applied their formulation with a realistic average orbital repeat time (24 h minus 246.8 s) [*Agnew and Larson*, 2007], and computed a predicted S2 propagation period of 174.5 days. This is in very close agreement with the peak observed in Figure 4 (~175 days). Thus, this result is the first confirmation of the propagation of tidal ATML using real data and provides clear evidence that the combination of nontidal plus S1+S2 ATML (solution 9) reduces some of the unexplained seasonal signals identified in previous studies [e.g., *Dong et al.*, 2002].

[44] Additionally, resolving ambiguities to integer values has a minimizing effect on the magnitude of the propagated signals. The stacked spectrum of the ambiguity free version of the nontidal plus S1+S2 minus nontidal only differences is provided in Figure 4 (red line). While the white noise magnitude of the difference is lower for the ambiguity free case, the power law noise component and the magnitude of the propagated signals, including the noticeable 6th harmonic, is clearly greater. This is in agreement with the results first shown by M. A. King and C. S. Watson (Long GPS coordinate time series: Multipath and geometry effects, submitted to *Journal of Geophysical Research*, 2009), who compared ambiguity free and fixed simulations, and analyses of real data, to quantify low-frequency variability induced by near field multipath and time variable network geometry. We discuss the propagation of the tidal components of ATML further in section 5.

4.2. Tropospheric Modeling

[45] *Steigenberger et al.* [2009] concluded that the combination of GMF mapping function and GPT hydrostatic delay modeling yielded solutions with smaller RMS than the VMF1 mapping functions with the ECMWF-derived ZHD values. At first, this seems counterintuitive, since the GMF is an empirical fit to the VMF1, hence should be less accurate, and the GPT is an empirical fit to global pressure fields, hence should be less accurate than using ECMWF-
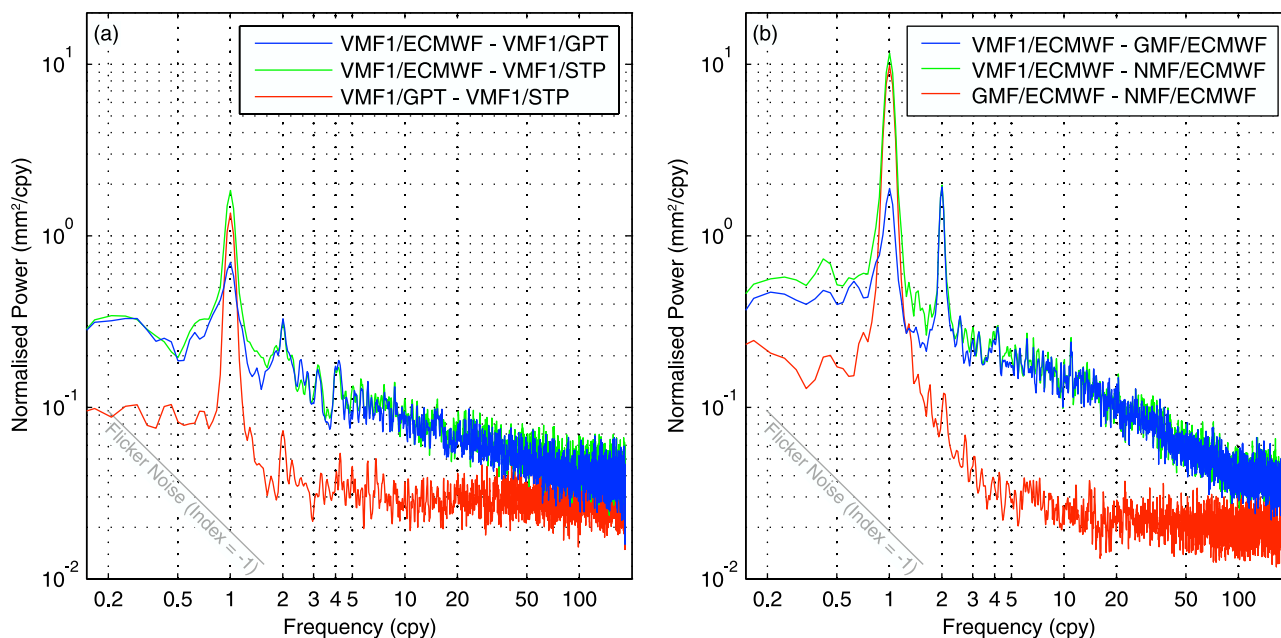
Figure 5. Stacked power spectra of height differences between solutions using (a) the VMF1 mapping function and different a priori ZHD derived from ECMWF, GPT, and STP and (b) the ECMWF ZHD and different mapping functions, VMF1, GMF, and NMF. In all cases, ATML (nontidal plus S1+S2) was applied at the observation level.

derived values for the a priori ZHD. Both *Kouba* [2008] and *Steigenberger et al.* [2009] speculated that this might be explained by destructive interference between mapping function errors and ATML deformation, where the latter remained unmodeled in their analyses. We revisit this issue by looking at solutions where we change first the mapping function, then the a priori ZHD model. In all cases, we model the nontidal and tidal ATML at the observation level, thereby removing the uncertainty in the results of previous studies that did not model this phenomenon.

[46] The up component of the white noise only analysis of solutions with VMF1/ECMWF, GMF/GPT, NMF/STP without ATML applied (solutions 1, 2 and 3) support their earlier findings, with the VMF1/ECMWF solution showing the highest white noise magnitudes. However, when ATML is applied at the observation level (solutions 9, 13 and 16) it becomes clear that the VMF1/ECMWF solution has less noise in all components for each noise model presented in Table 1. This is also the case when ATML is applied as a daily averaged value, where the power law noise on the vertical component is smaller for the VMF1/ECMWF solutions than for the GMF/GPT solutions.

4.2.1. A Priori ZHD Model

[47] Can the GPS analyses be improved by using a more accurate a priori model for the ZHD than the empirical GPT model? *Steigenberger et al.* [2009] found that when the mapping function was held constant (VMF1 or GMF) the solutions using the GPT had better repeatability than those using the ECMWF-derived a priori ZHD. We reassess this in the frequency domain by computing average spectra of stacked spectra of coordinate differences (at each site) between solutions using the VMF1 with the ZHD modeled a priori using STP, GPT or ECMWF-derived values.

[48] Figure 5a shows our stacked spectra of height difference spectra. The differences between GPT and STP (red line) essentially only occur at the annual period, with a flat, low power level at all higher frequencies.

[49] Conversely, differences between ECMWF and GPT occur over a large range of frequencies (blue line) in addition to the annual period. Thus, considerable analysis error can be removed by using a more sophisticated a priori ZHD model than the GPT.

4.2.2. Mapping Functions

[50] Here we consider the effect of the mapping function in solutions using ECMWF-derived a priori ZHD. The stacked spectra of our estimated height difference spectra between VMF1, GMF and NMF are shown in Figure 5b. The principal difference between GMF and NMF is at the annual period, again with little power at higher frequencies. The difference between VMF1 and GMF again spans a wide range of frequencies in addition to the annual period, including a significant peak at the semiannual frequency. Note that the magnitude of the power is 3–10 times larger than the differences seen when using different models of ZHD (Figure 5a). This is a significant point, showing that when assessing global averaged improvements the gains in applying the VMF1 over using the empirical GMF are much larger than applying the ECMWF-derived ZHD over the empirical GPT.

[51] *Steigenberger et al.* [2009] found that the VMF1 mapping function yielded slightly smaller RMS than using the GMF when the same a priori ZHD was used. We contend that the differences in the spectral domain provide conclusive evidence that the high-frequency temporal variations of the VMF1 do yield significant improvements in GPS analyses. Figures 5a and 5b demonstrate that the
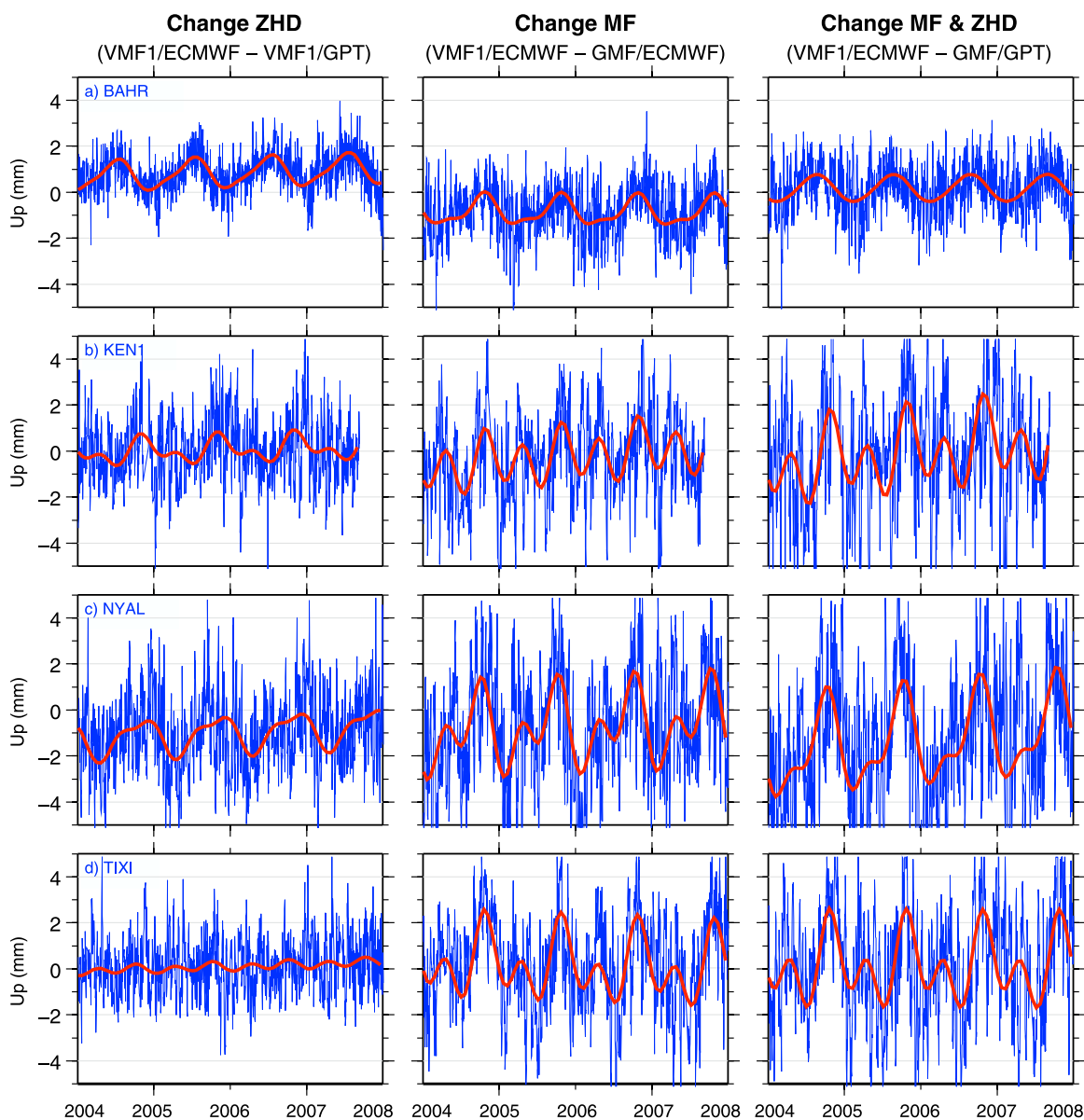
Figure 6. Time series showing differences in the up component between solutions using (left) VMF1/ECMWF to VMF1/GPT, (middle) VMF1/ECMWF to GMF/ECMWF, and (right) VMF1/ECMFW to GMF/GPT for (a) BAHR, (b) KEN1, (c) NYAL, and (d) TIXI. All solutions have ATML applied at the observation level (nontidal plus S1+S2). The red line is a best fit to the height differences for a model with solar annual and semiannual periodic terms.

empirical models of GMF and GPT capture only the long-wavelength features of the atmospheric variations.

4.2.3. Combined Effect

[52] It is clear that the use of different mapping functions and a priori ZHD models causes differences in the annual periodic signals in coordinate time series. The phases of these differences are not always the same. Figure 6 shows the height differences computed between solutions where first the a priori ZHD model was varied (always using VMF1 as the mapping function), then the mapping function (always using ECMWF as the a priori ZHD), then finally the combined differences of VMF1/ECMWF minus GMF/GPT. It now becomes apparent that the relative contributions of improved modeling of ZHD and/or mapping

function are actually site specific. In the case of Bahrain, using the GPT to model the annual pressure variations yields improvements of comparable magnitude to those derived by using the more sophisticated mapping function, whereas at the other sites the mapping function introduces more significant differences at both annual and semiannual frequencies. The interference of the annual variations contributed by the ZHD modeling and the mapping function is constructive at Ny-Ålesund, resulting in a combined annual variation of 1.9 mm amplitude. If one now assumes that the VMF1/ECMWF is the more accurate analysis approach, then the right column of Figure 6 shows the error that can be removed from GPS analysis by using VMF1/ECMWF rather than GMF/GPT. The spatial variabilities in the
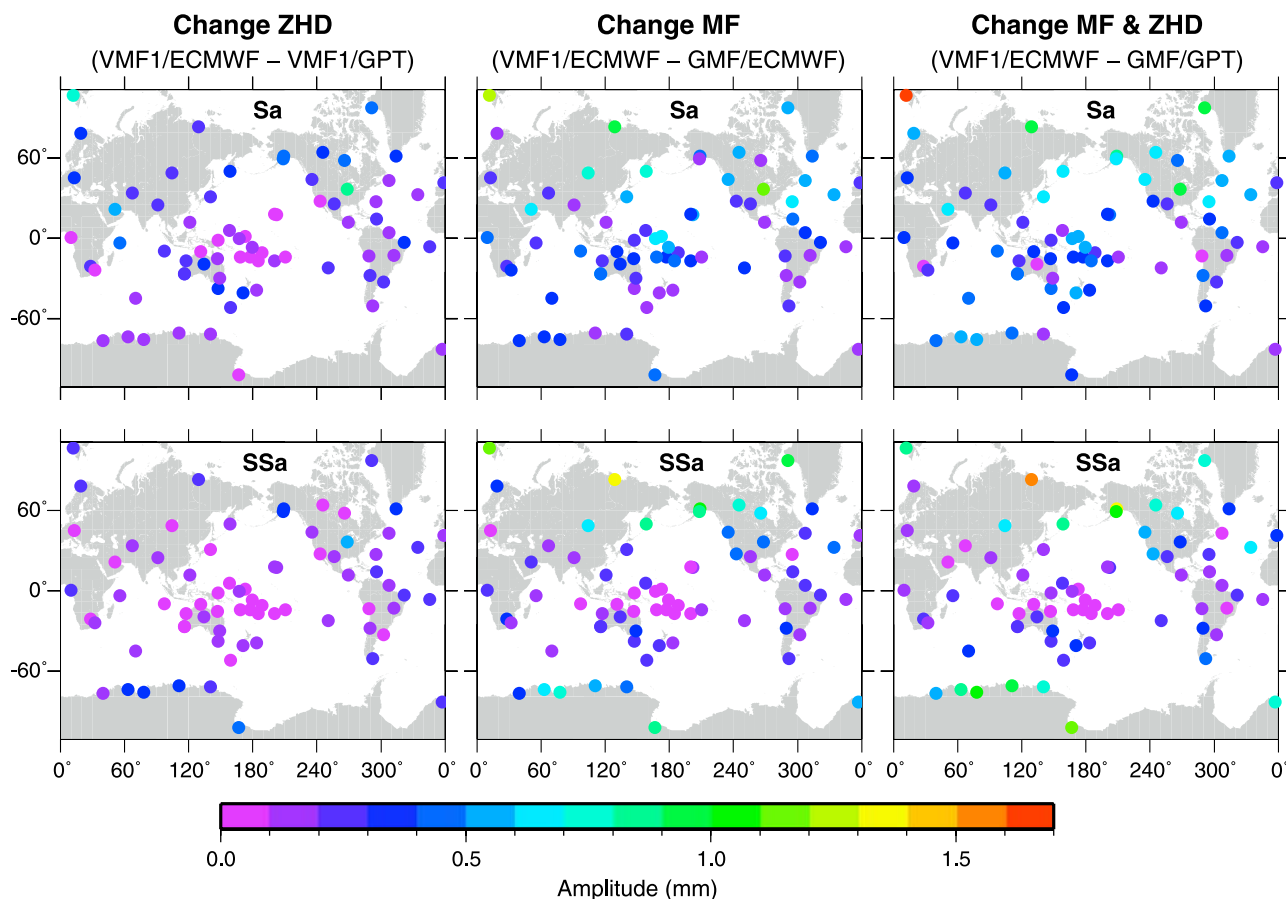
Figure 7. Amplitudes of annual and semiannual signals in solution differences using (left) ECMWF or GPT, (middle) VMF1 or GMF, and(right) VMF1/ECMFW or GMF/GPT. All solutions have ATML applied at the observation level (nontidal plus S1+S2).

amplitudes of annual and semiannual variations in the differences are shown in Figure 7.

5. Anomalous Periodic Signals

[53] *Ray et al.* [2008] presented stacked spectra of 167 GPS sites, derived from the weekly SINEX file solutions of the IGS. They noticed spectral peaks and a comb of harmonics that coincided with a so-called "GPS draconitic year" (abbreviated here as dy), being the 351.4 days required for a GPS orbit to repeat its inertial orientation with respect to the sun. The energy found at this period and its harmonics was not found in solutions from other space geodetic techniques nor geophysical data [*Ray et al.*, 2008]. Given that this period is close to the solar year (365.25 days), it is likely that the probable spurious draconitic signals will bias estimates of real geophysical phenomena that operate at seasonal (solar) timescales (for example, seasonal hydrological cycles). *Ray et al.* [2008] suggested that the causes for the draconitic signals lie in spurious aliasing and/or orbital errors or aliasing/propagation of site-dependent effects such as multipath.

5.1. Tidal ATML

[54] As shown in section 4.1.3, we have demonstrated using real data that failure to model the diurnal and

semidiurnal components of ATML can induce propagation of these tidal signals to distinct low-frequency signals with periods of ∼350–355 days and ∼175 days, with some evidence of higher harmonics (e.g., 58.5 days, Figure 4). These periods match closely those found by *Ray et al.* [2008], suggesting that at least some of the energy at draconitic periods identified by *Ray et al.* [2008] are derived from the absence of modeling of the S1 and S2 atmospheric tides in the IGS SINEX file solutions. We also see spectral peaks up to at least the 7th harmonic in our stacked time series (Figure 8).

[55] We now investigate the spatial variability and frequency dependence of the propagation effects of not modeling the atmospheric tides. We use the VMF1/ECMWF solutions with nontidal ATML and compute coordinate differences between solutions with (1) S1+S2 modeled, (2) only S1 modeled, (3) only S2 modeled, and (4) neither S1 nor S2 modeled. The differences provide insight into the relative contributions of each of the tidal signals. Using Bahrain as an example (Figure 9), we show the time domain and amplitude spectra of solution differences to highlight the influence of S1+S2, S1-only and S2-only. When applying S1+S2 at this site we observe the mitigation of a broad peak near 1 cycle per draconitic year (cpdy), and a clear, narrow peak at 2 cpdy (Figure 9a). Although only 0.6 mm in amplitude, the signal is very well resolved in the time series
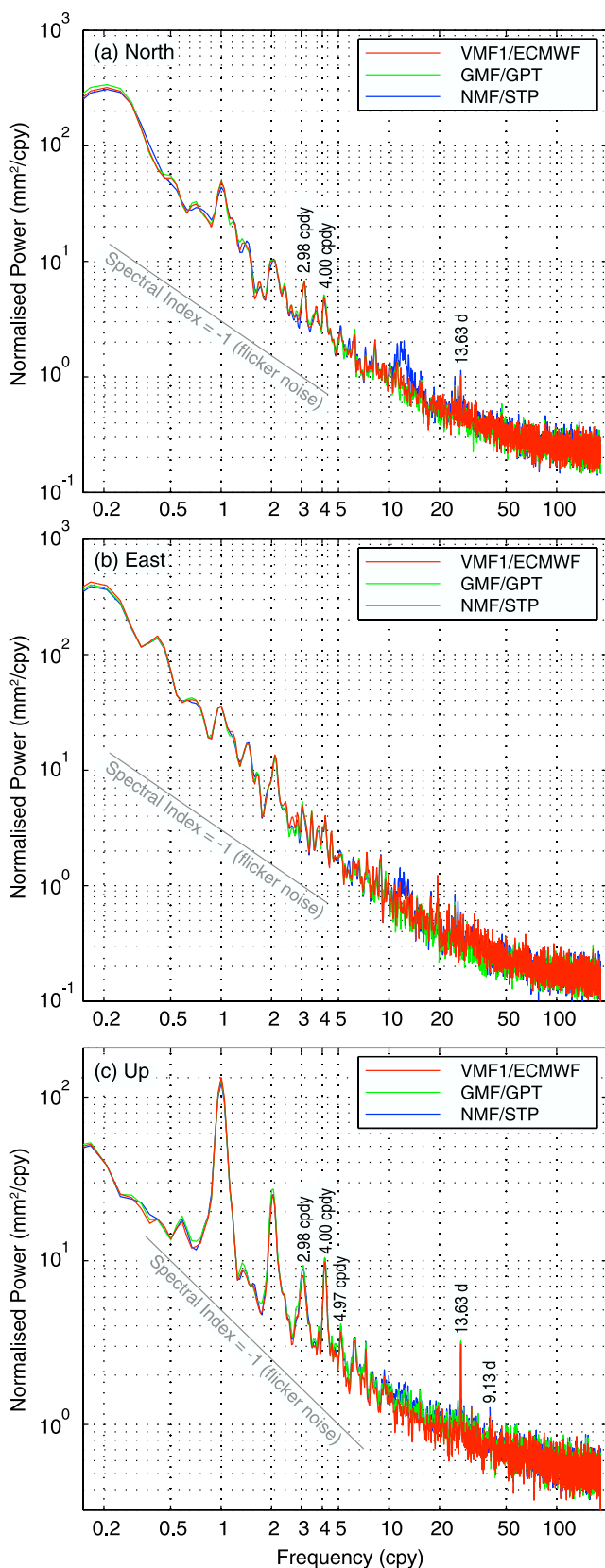
Figure 8. Stacked spectra of our VMF1/ECMWF, GMF/ GPT, and NMF/STP solutions with ATML (nontidal plus S1+S2) applied at the observation level for (a) north, (b) east, and (c) vertical components.

of height differences, and is ~60% of the vertical ATML tidal amplitudes at this site (1.1 mm and 0.9 mm for S1 and S2, respectively). The S1-only and S2-only contributions are shown in Figures 9b and 9c, respectively. We note that at Bahrain, the S1 tide contributes around 66% of the power at 2 cpdy, while the S2 tide contributes the remaining one third. The latter also contributes the majority of the power to the broad annual peak in the difference spectra.

[56] We concur with *Ray et al.* [2008] that given the length of our time series, we have limited frequency resolution around 1 cpdy and hence are unable to distinguish between solar annual and draconitic annual frequencies for the broad annual peaks seen in Figure 8. We have better resolution in the stacked spectra of these differences (Figure 4), indicating that the energy is indeed centered on the draconitic annual frequency.

[57] Using the same solution differences, we compute the site-specific amplitude of two periodic signals with frequency of 1 and 2 cpy, respectively. Plotting the draconitic semiannual amplitude versus latitude reveals a curious pattern. The combined influence of S1 and S2 shows two peaks in the midlatitudes, similar to a degree 3 zonal harmonic pattern (Figure 10a). When separated, the contributions of S1 and S2 show a similar, double-peaked pattern where S1 and S2 contribute roughly equally (Figures 10b and 10c, respectively). While the basic propagation mechanisms for S1 and S2 are thought to be reasonably well understood (see section 4.1.3) the mechanism by which the propagation interacts within a global solution using the double-differenced approach and simultaneous estimation of satellite orbit parameters is not yet clear and is beyond the scope of this paper. We do however note that ambiguity resolution has a minimizing effect on the magnitude of the S1 and S2 error propagation (as shown in Figure 4).

[58] Given our finding that unmodeled tidal ATML can explain some of the spurious energy present at draconitic frequencies observed by *Ray et al.* [2008], we further investigate our best solution (VMF1/ECMWF nontidal plus S1+S2) for additional energy at harmonics of the draconitic year. As shown in Figure 8, our best solution still contains spectral peaks identifiable up to the 7th harmonic. Smaller, less pronounced peaks with respect to the surrounding noise floor are evident in the north component (Figure 8a, a clear improvement in our solutions compared with those shown by *Ray et al.* [2008]), with less evidence for these signals in east (Figure 8b). These peaks are not present in the spectra of differenced time series, indicating that the propagated signals are equally present in solutions using different mapping functions and a priori ZHD. Therefore, one can conclude that the propagated signals are not driven by mapping function or ZHD errors.

[59] We note the presence of energy across north, east and up components with a period of ~13.63 days and also in the up component with period ~9.13 days. The ~13.63 days peak could indicate a propagated signal(s) caused by mismodeling of the M2 or O1 constituents within ocean tide loading or solid Earth tide models used in our analysis [*Penna et al.*, 2007]. Equally plausible however is that this signal results from purely mismodeling deformation coinciding with the Mf tidal constituent (13.66 days). The ~9.13 days peak is almost certainly a propagated signal
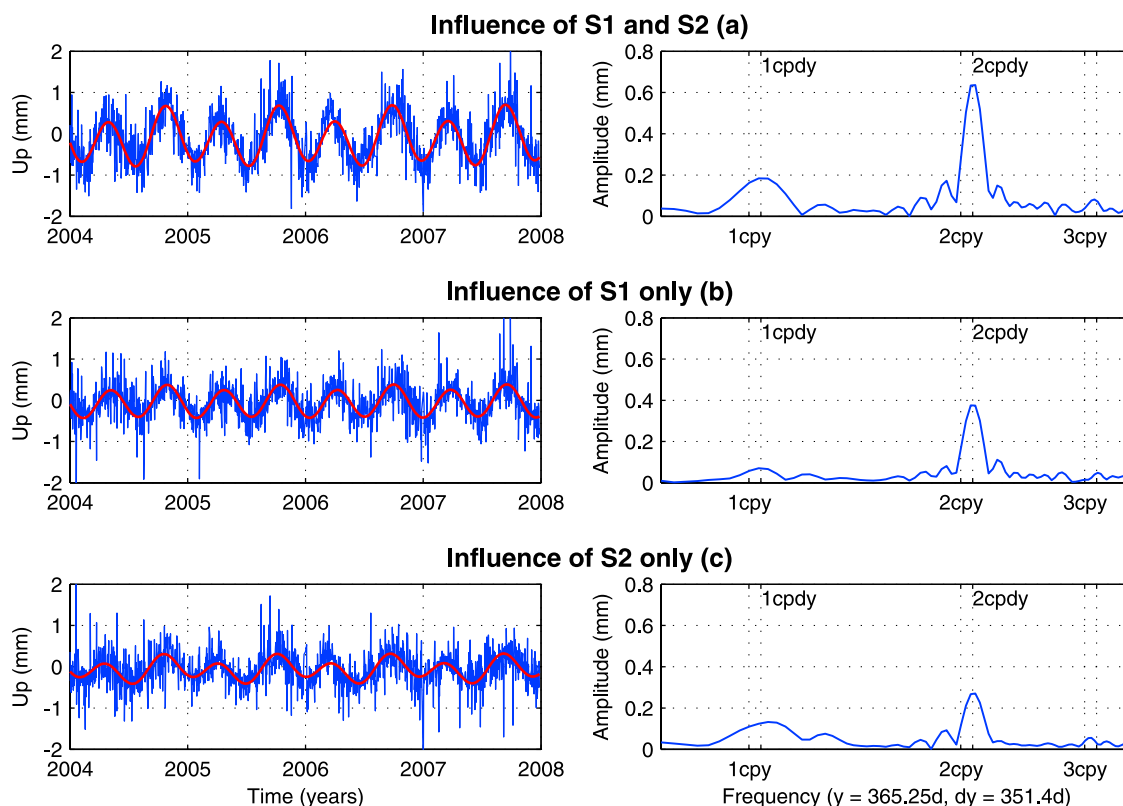
Figure 9. Effect of modeling of atmospheric tides on height estimates at Bahrain as demonstrated by calculating the difference in heights from solutions that treat the tidal ATML differently. (a) Influence of S1 and S2 (solution 9 minus solution 1), (b) influence of S1 only (solution 9 minus solution with S2 only), and (c) influence of S2 only (solution with S1 only minus solution 1). (left) Time domain (red line is a best fitting GPS draconitic annual and semiannual model) and (right) amplitude spectra.

resulting from the repeat orbit effect with respect to mismodeled energy in the N2 and Q1 constituents [*Penna and Stewart*, 2003].

5.2. Ambiguity Resolution

[60] We now investigate the impact on the GPS coordinate estimates of not resolving the phase ambiguities to integer values. We use solutions with VMF1/ECMWF, nontidal and S1+S2 ATML and compute differences between the ambiguity-free and ambiguity-fixed solutions (where fixed means resolved to integers). The stacked spectra for the free-fixed difference, for each component, provides a remarkable result (Figure 11). Here we observe that failure to fix ambiguities leads to a significant amplification in the expression of the spurious draconitic harmonics, combined with significant time-correlated noise and additional propagation into periods around ∼14 days. For example, the peak at 14.16 days is now quite clear, perhaps indicating that the use of 24 h session lengths causes propagation of a mismodeled O1 signal when ambiguities are not resolved. The combined white noise and power law metrics for this difference solution (Table 2) show a remarkably high level of power law noise with spectral indices close to flicker noise. The IGS solution analysis presented by *Ray et al.* [2008] probably included solutions with unresolved ambiguities, thus explaining the

greater relative magnitude of the harmonic peaks observed in *Ray et al.*'s [2008] study.

6. Conclusions

[61] The application of so-called nontidal ATML, filtered with a low-pass filter to remove remnant power at subdaily frequencies, along with the application of S1+S2 tidal ATML, leads to improved GPS coordinate time series metrics thus providing the most precise determination of parameters of geophysical interest. Linearly interpolating between 6-hourly ATML deformation data that still contain partial tidal power is shown to be worse than applying the filtered nontidal ATML plus the addition of S1+S2 ATML, introducing significant time-correlated noise and spurious periodic signals into the low-frequency end of the spectrum. We find no evidence in site coordinate estimates that applying nontidal ATML at the observation level yields more accurate estimates compared to applying a daily averaged value a posteriori prior to aligning the free-network solutions with the ITRF2005.

[62] Both the VMF1 mapping function and the time-varying a priori ZHD derived from the ECMWF numerical weather model yield more precise GPS coordinate time series compared to empirical approaches of other mapping functions and a priori ZHD. This holds whether ATML is applied at the observation level or as a daily averaged value.
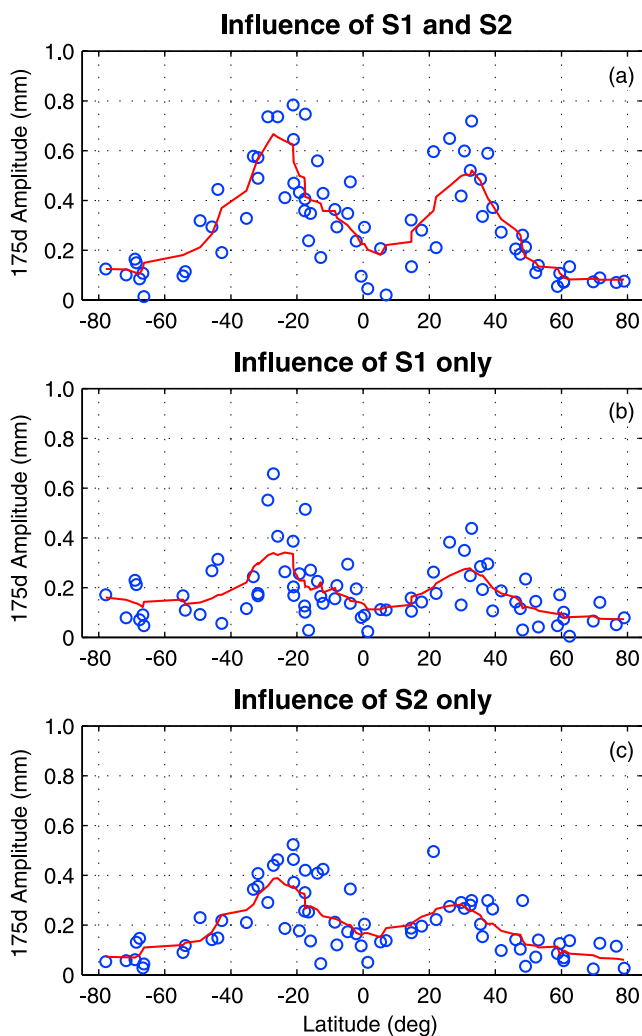
Figure 10. Amplitude of the GPS draconitic semiannual signals as a function of latitude. (a) Influence of S1 and S2, (b) influence of S1 only, and (c) influence of S2 only. Red lines are nine-point moving averages.

We note that failure to account for the seasonal variations as evidenced within the VMF1 and ECMWF-derived ZHD results in significant spurious energy remaining at seasonal periods (dominated by solar annual and semiannual). Thus, potential biases of inferred seasonal geophysical phenomena may result.

[63] An unexpected result of this study was the magnitude of the signal propagation when failing to model the S1 and S2 tidal ATML. Demonstrating this for the first time using real data processed using the double-difference approach, we show that failure to model tidal ATML induces low-frequency spurious signals with periods of ~350 days and ~175 days (1 and 2 cycles per ''GPS draconitic'' year, respectively). The very high admittance (ratio of input amplitude to aliased amplitude) indicates that the failure to model tidal ATML in current GPS analyses will lead to biased estimates of real periodic geophysical signals. This places clear emphasis on the requirement to revisit and improve the modeling of tidal ATML (and indeed other subdaily geophysical models required in GPS analyses).
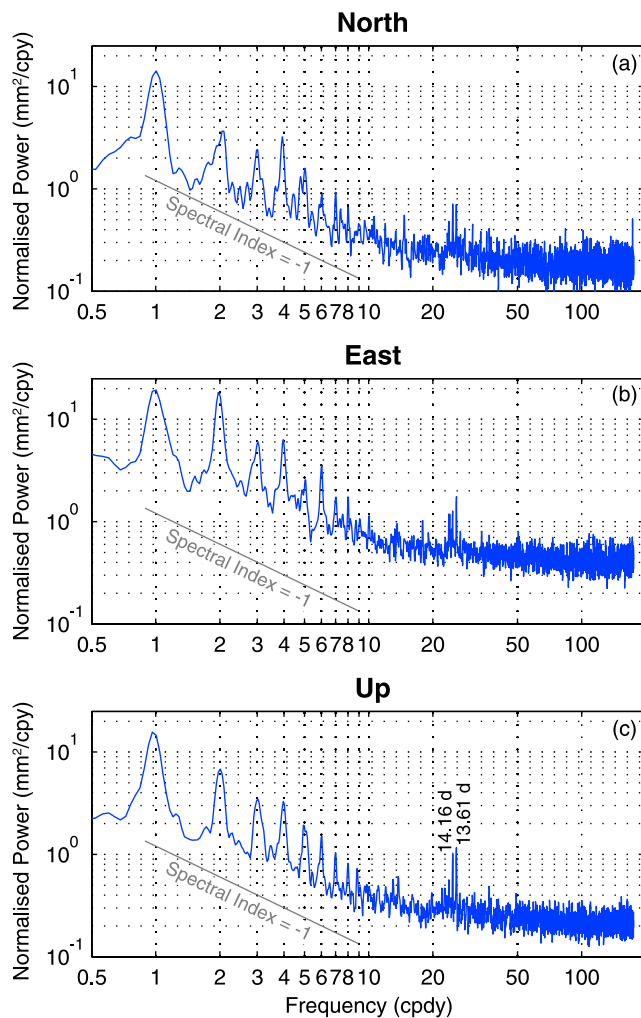

Figure 11. Stacked spectra from the ambiguity fixed-free solution difference (both VMF1/ECMWF nontidal plus S1+S2) for (a) north, (b) east, and (c) up components. Note the change in frequency units to cycles per 351.4 days.

[64] Also unexpected was the magnitude of the reduction in spurious periodic energy resulting from fixing ambiguities in the GPS analyses. We conclude that a component of the energy observed at GPS draconitic frequencies by *Ray et al.* [2008] results from (1) not modeling tidal ATML and (2) some combination of fixed and free ambiguity resolution solutions within the combined IGS SINEX files. The driver of the energy seen by *Ray et al.* [2008] (in addition to not modeling tidal ATML), and that is still observed at these frequencies in our best solution, remains an open question.

Table 2. Combined White and Power Law Noise Metrics From the Ambiguity-Fixed Minus Ambiguity-Free Solution Difference[a]

Solution[b]	WN			PL Magnitude			Spectral Index		
	N	E	U	N	E	U	N	E	U
9-9*	1.35	2.26	2.38	2.99	5.18	6.10	−0.90	−0.88	−0.95

[a]Both VMF1/ECMWF nontidal plus S1+S2.
[b]Solution 9* is the same analysis strategy as solution 9 but the ambiguities were not resolved to integers.

King and Watson (submitted manuscript, 2009) show that near field multipath is a potential contributor as well as the time variable constellation geometry.

[65] From this analysis at the global scale, we suggest that high-accuracy analyses of GPS data should incorporate integer ambiguity resolution and utilize the VMF1 mapping function and ray-traced a priori ZHD values, as well as applying both nontidal and tidal ATML, despite the added complexity of incorporating these models into current software packages. Failure to do so will result in the generation of solutions of inferior accuracy, with a subsequent reduction in the ability to provide meaningful geophysical interpretation.

References

Agnew, D. C., and K. M. Larson (2007), Finding the repeat time of the GPS constellation, *GPS Solut.*, 11, 71–76, doi:10.1007/s10291-006-0038-4.

Altamimi, Z., X. Collilieux, J. Legrand, B. Garayt, and C. Boucher (2007), ITRF2005: A new release of the International Terrestrial Reference Frame based on time series of station positions and Earth Orientation Parameters, *J. Geophys. Res.*, 112, B09401, doi:10.1029/2007JB004949.

Bevis, M., S. Businger, T. Herring, C. Rocken, R. Anthes, and R. Ware (1992), GPS Meteorology: Remote sensing of atmospheric water vapor using the Global Positioning System, *J. Geophys. Res.*, 97(D14), 15,787–15,801.

Bock, Y., et al. (1993), Detection of crustal deformation from the Landers earthquake sequence using continuous geodetic measurements, *Nature*, 361, 337–340, doi:10.1038/361337a0.

Boehm, J., and H. Schuh (2004), Vienna mapping functions in VLBI analyses, *Geophys. Res. Lett.*, 31, L01603, doi:10.1029/2003GL018984.

Boehm, J., B. Werl, and H. Schuh (2006a), Troposphere mapping functions for GPS and very long baseline interferometry from European Centre for Medium-Range Weather Forecasts operational analysis data, *J. Geophys. Res.*, 111, B02406, doi:10.1029/2005JB003629.

Boehm, J., A. Niell, P. Tregoning, and H. Schuh (2006b), Global mapping function (GMF): A new empirical mapping function based on numerical weather model data, *Geophys. Res. Lett.*, 33, L07304, doi:10.1029/2005GL025546.

Boehm, J., R. Heinkelmann, and H. Schuh (2007), Short Note: A global model of pressure and temperature for geodetic applications, *J. Geod.*, 81, 679–683, doi:10.1007/s00190-007-0135-3.

Dach, R., U. Hugentobler, P. Freidez, and M. Meindl (2007), Bernese GPS software version 5.0, Astron. Inst., Univ. of Berne, Berne, Jan.

Darwin, G. H. (1882), On variations in the vertical due to elasticity of the Earth's surface, *Philos. Mag.*, 14(90), 409–427.

Dong, D., P. Fang, Y. Bock, M. K. Cheng, and S. Miyazaki (2002), Anatomy of apparent seasonal variations from GPS-derived site position time series, *J. Geophys. Res.*, 107(B4), 2075, doi:10.1029/2001JB000573.

Farrell, W. E. (1972), Deformation of the Earth by surface loads, *Rev. Geophys.*, 10, 761–797, doi:10.1029/RG010i003p00761.

Feigl, K. L., et al. (1993), Space geodetic measurement of crustal deformation in central and southern California, 1984–1992, *J. Geophys. Res.*, 98(B12), 21,677–21,712, doi:10.1029/93JB02405.

Herring, T. A. (1992), Modeling atmospheric delays in the analysis of space geodetic data, in *Refraction of Transatmospheric Signals in Geodesy: Proceedings of the Symposium, The Hague, The Netherlands, May 19–22, 1992, Publ. Geod.*, vol. 36, edited by J. C. De Munk and T. A. Spoelstra, pp. 157–164, Neth. Geod. Comm., Delft, Netherlands.

Herring, T. A., R. W. King, and S. C. McClusky (2008), Introduction to GAMIT/GLOBK, report, Mass. Inst. of Technol., Cambridge.

Kouba, J. (2008), Testing of global pressure/temperature (GPT) model and global mapping function (GMF) in GPS analyses, *J. Geod.*, 83(3–4), 199–208, doi:10.1007/s00190-008-0229-6.

Mao, A., C. G. A. Harrison, and T. H. Dixon (1999), Noise in GPS coordinate time series, *J. Geophys. Res.*, 104, 2797–2816, doi:10.1029/1998JB900033.

Milne, G. A., J. L. Davis, J. X. Mitrovica, H.-G. Scherneck, J. M. Johansson, M. Vermeer, and H. Koivula (2001), Space-geodetic constraints on glacial isostatic adjustment in Fennoscandia, *Science*, 291, 2381–2385, doi:10.1126/science.1057022.

Niell, A. E. (1996), Global mapping functions for the atmosphere delay at radio wavelengths, *J. Geophys. Res.*, 101, 3227–3246, doi:10.1029/95JB03048.

Penna, N. T., and M. P. Stewart (2003), Aliased tidal signatures in continuous GPS height time series, *Geophys. Res. Lett.*, 30(23), 2184, doi:10.1029/2003GL018828.

Penna, N. T., M. A. King, and M. P. Stewart (2007), GPS height time series: Short-period origins of spurious long-period signals, *J. Geophys. Res.*, 112, B02402, doi:10.1029/2005JB004047.

Petrov, L., and J.-P. Boy (2004), Study of the atmospheric pressure loading signal in very long baseline interferometry observations, *J. Geophys. Res.*, 109, B03405, doi:10.1029/2003JB002500.

Ponte, R. M., and R. D. Ray (2002), Atmospheric pressure corrections in geodesy and oceanography: A strategy for handling air tides, *Geophys. Res. Lett.*, 29(24), 2153, doi:10.1029/2002GL016340.

Press, W. H., S. A. Teukolsky, W. T. Vetterling, and B. P. Flannery (1992), *Numerical Recipes in FORTRAN 77: The Art of Scientific Computing*, 2nd ed., Cambridge Univ. Press, Cambridge, U. K.

Ray, J., Z. Altamimi, X. Collieux, and T. van Dam (2008), Anomalous harmonics in the spectra of GPS position estimates, *GPS Solut.*, 12, 55–64, doi:10.1007/s10291-007-0067-7.

Saastamoinen, J. (1972), Atmospheric correction for the troposphere and stratosphere in radio ranging of satellites, in *The Use of Artificial Satellites for Geodesy in Geodesy, Geophys. Monogr. Ser.*, vol. 15, edited by S. W. Henriksen, A. Mancini, and B. H. Chovitz, pp. 247–251, AGU, Washington, D. C.

Scargle, J. D. (1982), Studies in astronomical time series analysis: II. Statistical aspects of spectral analysis of unevenly spaced data, *Astrophys. J.*, 263, 835–853, doi:10.1086/160554.

Sella, G. F., S. Stein, T. H. Dixon, M. Craymer, T. S. James, S. Mazzotti, and R. K. Dokka (2007), Observation of glacial isostatic adjustment in "stable" North America with GPS, *Geophys. Res. Lett.*, 34, L02306, doi:10.1029/2006GL027081.

Snay, R., M. Cline, W. Dillinger, R. Foote, S. Hilla, W. Kass, J. Ray, J. Rohde, G. Sella, and T. Soler (2007), Using global positioning system-derived crustal velocities to estimate rates of absolute sea level change from North American tide gauge records, *J. Geophys. Res.*, 112, B04409, doi:10.1029/2006JB004606.

Steigenberger, P., J. Boehm, and V. Tesmer (2009), Comparison of GMF/GPT with VMF1/ECMWF and implications for atmospheric loading, *J. Geod.*, doi:10.1007/s00190-009-0311-8, in press.

Stewart, M. P., N. T. Penna, and D. D. Lichti (2005), Investigating the propagation mechanism of unmodelled systematic errors on coordinate time series estimated using least squares, *J. Geod.*, 79, 479–489, doi:10.1007/s00190-005-0478-6.

Tregoning, P., and T. A. Herring (2006), Impact of a priori zenith hydrostatic delay errors on GPS estimates of station heights and zenith total delays, *Geophys. Res. Lett.*, 33, L23303, doi:10.1029/2006GL027706.

Tregoning, P., and T. van Dam (2005a), Atmospheric pressure loading corrections applied to GPS data at the observation level, *Geophys. Res. Lett.*, 32, L22310, doi:10.1029/2005GL024104.

Tregoning, P., and T. van Dam (2005b), Effects of atmospheric pressure loading and seven-parameter transformations on estimates of geocenter motion and station heights from space geodetic observations, *J. Geophys. Res.*, 110, B03408, doi:10.1029/2004JB003334.

Tregoning, P., G. Ramillien, H. McQueen, and D. Zwartz (2009), Glacial isostatic adjustment and nonstationary signals observed by GRACE, *J. Geophys. Res.*, 114, B06406, doi:10.1029/2008JB006161.

van Dam, T., and T. Herring (1994), Detection of atmospheric pressure loading using very long baseline interferometry measurements, *J. Geophys. Res.*, 99, 4505–4517, doi:10.1029/93JB02758.

van Dam, T., G. Blewitt, and M. Heflin (1994), Atmospheric pressure loading effects on Global Positioning System coordinate determinations, *J. Geophys. Res.*, 99, 23,939–23,950, doi:10.1029/94JB02122.

Watson, C., P. Tregoning, and R. Coleman (2006), Impact of solid Earth tide models on GPS coordinate and tropospheric time series, *Geophys. Res. Lett.*, 33, L08306, doi:10.1029/2005GL025538.

Williams, S. D. P. (2008), CATS: GPS coordinate time series analysis software, *GPS Solut.*, 12, 147–153, doi:10.1007/s10291-007-0086-4.

Williams, S. D. P., Y. Bock, P. Fang, P. Jamason, R. M. Nikolaidis, L. Prawirodirdjo, M. Miller, and D. J. Johnson (2004), Error analysis of continuous GPS position time series, *J. Geophys. Res.*, *109*, B03412, doi:10.1029/2003JB002741.

Wöppelmann, G., B. M. Miguez, M.-N. Bouin, and Z. Altamimi (2007), Geocentric sea-level trend estimates from GPS analyses at relevant tide gauges world-wide, *Global Planet. Change*, *57*(3–4), 396–406, doi:10.1016/j.gloplacha.2007.02.002.

Zhang, J., Y. Bock, H. Johnson, P. Fang, S. Williams, J. Genrich, S. Wdowinski, and J. Behr (1997), Southern California permanent GPS geodetic Array: Error analysis of daily position estimates and site velocities, *J. Geophys. Res.*, *102*, 18,035–18,055, doi:10.1029/97JB01380.

————————————

P. Tregoning, Research School of Earth Sciences, Australian National University, OHB-A, Building 61A, Mills Road, Canberra 0200, ACT, Australia. (paul.tregoning@anu.edu.au)

C. Watson, Surveying and Spatial Science Group, School of Geography and Environmental Studies, Private Bag 76, University of Tasmania, Hobart, Tasmania 7001, Australia. (cwatson@utas.edu.au)